Available online at www.sciencedirect.com

SCIENCE DIRECT®

International Journal of Heat and Mass Transfer 47 (2004) 4479–4489

International Journal of HEAT and MASS TRANSFER

www.elsevier.com/locate/ijhmt

Numerical modeling of heat and mass transfer in porous medium during combined hot air, infrared and microwaves drying

P. Salagnac *, P. Glouannec, D. Lecharpentier

Laboratoire d'Etudes Thermiques, Energétiques et Environment, UBS, Centre de Recherche, Rue St Maudé, BP 92116, 56321 Lorient Cedex, France

Received 17 January 2002

Abstract

This study deals with numerical modeling of the hygrothermal behaviour of a rectangular-shaped porous material during combined drying. This material is submitted on its upper side both a hot air flow as well as infrared and microwave radiations. The one-dimensional physical model describing heat and mass transfers allows accessing temperature, moisture content and pressure fields. Energy inputs induced by the electromagnetic radiation are determined by the Lambert–Beer law. Comparison of experimental and simulated results on cellular concrete shows the relevance of this model for studies on combined drying.

1. Introduction

Radiating technologies are particularly interesting in a drying operation in that they allow immediate and significant energy input to the product to be processed. However, the high power density applied to the material can significantly alter the usual drying kinetics and bring about important constraints. When using infrared, too high power density can cause caking phenomena. Microwave can also cause high pressures within the material, which increase mass transfers but also generate significant mechanical stresses [1–4].

Traditional drying methods are well documented by numerous experimental and theoretical studies, which is not the case with so-called mixed processes (convection and radiation) [4–13]. The purpose of the current research in our laboratory is to optimise the combined use of microwaves and infrared in a drying operation. Also, we have developed a pilot and a numerical model allowing assessing the evolution of temperature, moisture content and pressure during the drying of a porous material placed in the test kiln.

This paper essentially deals with the validation of the simulations. First comes a presentation of the physical model designed to describe mass and heat transfer within the porous material. We then introduce the energy inputs generated by both types of electromagnetic radiation. The second part describes the drying pilot. This is followed by a presentation of numerical simulation results, which will be compared to combined drying tests conducted on cellular concrete.

2. Mathematical model

This modeling was developed in order to simulate the hygrothermal behaviour of a parallelopidal porous medium. The material is supposed rigid and non-saturated with a hygroscopic and capillary behaviour. Fig. 1 features the boundary conditions corresponding to the experimental survey. Mass and heat transfers are supposed one-dimensional. The upper side ($x = 0$) of the material is subjected to a convective flow and can undergo a microwave and/or a thermal radiation within the

---

[*] Corresponding author.

0017-9310/$ - see front matter © 2004 Elsevier Ltd. All rights reserved.
doi:10.1016/j.ijheatmasstransfer.2004.04.015

Nomenclature

a_w	water activity
C	mass fraction of the vapour in the gaseous phase
C_p	specific heat at constant pressure
d	penetration depth
D_v^{eff}	effective diffusivity coefficient of vapour
F_m	superficial evaporated mass flux
g	gravitational acceleration
h_c	convective heat transfer coefficient
h_r	radiative heat transfer coefficient
H_r	relative humidity
IR	Infrared
k	intrinsic permeability
k_{rl}	relative permeability of liquid phase
k_{rg}	relative permeability of gas phase
k_m	mass transfer coefficient
K	phase change volumetric rate
L	solid thickness
M	molecular weight
MW	Microwave
P_{atm}	atmospheric pressure
P_c	capillary pressure
P_i	pressure of the component i
$p_{v\infty}$	ambient partial vapour pressure
P_{vs}	saturated vapour pressure
R	gas constant/reflection coefficient
S	saturation
t	time
T	temperature
T_a	air temperature
T_f	film temperature
T_p	wall enclosure temperature
$\overline{V}$	mean filtration velocity
W	mass moisture content
x	sample depth

Greek symbols

α	infrared absorption coefficient
ΔH_b	differential heat of desorption
ΔH_v	latent heat of vaporisation
ε	porosity
ε_r'	dielectric permittivity
ε_r''	relative loss factor
ϕ_{so}	internal volumic power
Φ	power
κ	attenuation factor
λ^*	effective thermal conductivity
λ_0	free space wavelength
$\overline{\underline{\rho_i}}$	density of phase i
ρ_i^g	intrinsic average density of component i in gaseous phase
μ	dynamic viscosity
ν	kinematic viscosity

Superscripts

a	absorb
i	incident
t	transmit

Subscripts

a	air
g	gas
l	liquid water
s	solid
v	water vapour

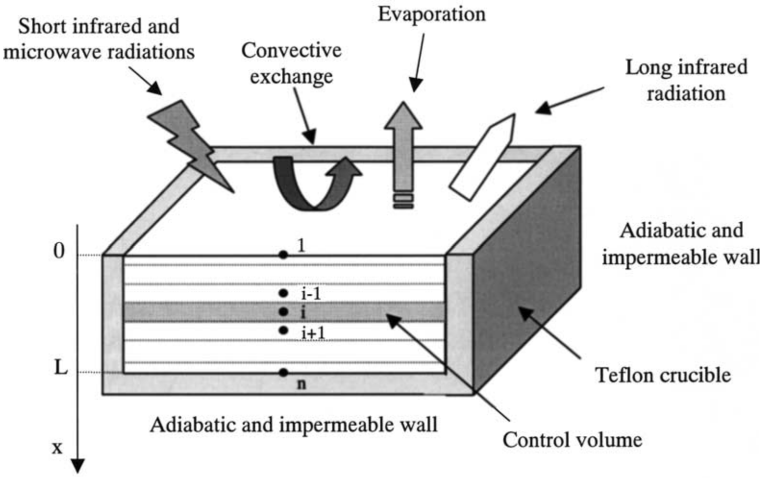

Fig. 1. Boundary conditions and spatial discretisation.

range of short infrared. The bottom side ($x = L$) is supposed impermeable and adiabatic or subjected to a given temperature.

2.1. Heat and mass transfer

The chosen model for the heat and mass transfers follows the macroscopic approach developed by Whitaker [14]. This model, based on the definition of elementary representative volume, has recently been investigated and appears to fit best the needs of our research [15–19]. The hygrothermal behaviour of the material is defined by three variables: temperature T, mass moisture content W and total pressure of the gaseous phase P_g.

2.1.1. Assumptions

The studied medium consists of three phases: solid (s), liquid (l) and gas (g). The liquid phase, consisting of free water and bound water, is supposed indissociable. Introducing a differential heat of sorption in the energy conservation equation takes into account the necessary energy input to the vaporisation of bound water. Moreover, one assumes that:

- the medium is homogeneous,
- the local thermodynamic equilibrium is achieved,
- the liquid phase is not compressible: $\rho_\ell = \text{constant}$,
- the gaseous phase consists of a perfect blend of gas: dry air (a) and vapour (v), whose equations read as follows:

$$P_i = \bar{\rho}_i^{g} \frac{R}{M_i} T \quad \text{for } i = (\text{a}, \text{v}) \quad \text{with}$$
$$P_g = P_a + P_v \quad \text{and} \quad \bar{\rho}_g^{g} = \bar{\rho}_a^{g} + \bar{\rho}_v^{g}, \tag{1}$$

- no chemical reactions within the material,
- radiation is negligible.

2.1.2. Governing equations

The hygrothermal behaviour of the material is described from mass and energy conservation equations, in addition to the diffusion laws.

2.1.2.1. Mass conservation equations

Dry air phase
$$\frac{\partial \bar{\rho}_a}{\partial t} + \nabla \cdot (\bar{\rho}_a^{g} \overline{\mathbf{V}}_a) = 0 \tag{2}$$

Vapour phase
$$\frac{\partial \bar{\rho}_v}{\partial t} + \nabla \cdot (\rho_v^{g} \overline{\mathbf{V}}_v) = K \tag{3}$$

Liquid phase
$$\frac{\partial \bar{\rho}_l}{\partial t} + \nabla \cdot (\rho_l \overline{\mathbf{V}}_l) = -K \tag{4}$$

These equations show the matter flows, which are derived from the Fick law for diffusion and by Darçy's generalised equations giving the mean filtration velocity fields of the liquid and gaseous phases.

- Liquid water flux

$$\begin{aligned}\rho_l \overline{\mathbf{V}}_l &= -\frac{\rho_l k k_{rl}}{\mu_l}(\nabla P_l - \bar{\rho}_l \mathbf{g}) \\ &= \frac{\rho_l k k_{rl}}{\mu_l} \nabla P_c - \frac{\rho_l k k_{rl}}{\mu_l}(\nabla P_g - \bar{\rho}_l \mathbf{g})\end{aligned} \tag{5}$$

Capillary pressure P_c is obtained from the desorption isotherms [16] through Kelvin's relation:

$$a_w = \frac{P_v}{P_{vs}} = \exp\left(\frac{-P_c}{\rho_l R T}\right) \tag{6}$$

- Vapour flux

$$\begin{aligned}\bar{\rho}_v^{g} \overline{\mathbf{V}}_v &= \bar{\rho}_v^{g} \overline{\mathbf{V}}_g - \bar{\rho}_g^{g} D_v^{\text{eff}} \nabla C \\ &= -\bar{\rho}_v^{g} \frac{k k_{rg}}{\mu_g}(\nabla P_g - \bar{\rho}_g^{g} \mathbf{g}) - \bar{\rho}_g^{g} D_v^{\text{eff}} \nabla C\end{aligned} \tag{7}$$

C being the mass fraction of the vapour in the gaseous phase, given by:

$$C = \frac{\bar{\rho}_v^{g}}{\bar{\rho}_a^{g} + \bar{\rho}_v^{g}} \tag{8}$$

- Dry air flux

$$\begin{aligned}\bar{\rho}_a^{g} \overline{\mathbf{V}}_a &= \bar{\rho}_g^{g} \overline{\mathbf{V}}_g - \bar{\rho}_v^{g} \overline{\mathbf{V}}_v \\ &= -\bar{\rho}_a^{g} \frac{k k_{rg}}{\mu_g}(\nabla P_g - \bar{\rho}_g^{g} \mathbf{g}) + \bar{\rho}_g^{g} D_v^{\text{eff}} \nabla C\end{aligned} \tag{9}$$

2.1.2.2. Energy conservation equation.

A reading of energy balance shows heat transfers through conduction, convection and phase change as well as energy inputs:

$$\begin{aligned}&\overline{\rho C_p} \frac{\partial T}{\partial t} + \left(\rho_l \overline{V}_l C_{p_l} + \bar{\rho}_a^{g} \overline{V}_a C_{p_a} + \bar{\rho}_v^{g} \overline{V}_v C_{p_v}\right) \cdot \nabla T \\ &\quad + \nabla(-\lambda^* \nabla T) + K(\Delta H_v + \Delta H_b) = \phi_{so}\end{aligned} \tag{10}$$

with $\overline{\rho C_p} = \bar{\rho}_s C_{p_s} + \bar{\rho}_l C_{p_l} + \bar{\rho}_v C_{p_v} + \bar{\rho}_a C_{p_a}$, the volumetric constant pressure heat capacity and λ^*, the effective thermal conductivity depending on moisture content. The necessary energy for the vaporisation of free and bound water is obtained by the phase change rate K Eq. (3), the latent heat of vaporisation ΔH_v and the differential heat of desorption ΔH_b.

2.1.2.3. System of equations.

After calculating the various matter flows according to the three state variables, one obtains a system of three tightly coupled highly nonlinear partial differential equations (Eqs. (11)–(13)). These equations feature the coefficients $\gamma_1, \gamma_2, \gamma_3$ and D_i^j described in Appendix A.

The moisture content equation W is established from the relations (3) and (4).

$$\begin{aligned}&\frac{\partial W}{\partial t} + \nabla \cdot \Bigg[\frac{1}{\rho_s}[(D_l^T + D_v^T)\nabla T + (D_l^W + D_v^W)\nabla W \\ &\quad + (D_l^P + D_v^P)\nabla P_g + (D_l^g + D_v^g) g]\Bigg] = 0\end{aligned} \tag{11}$$

The equation for the total pressure of the gaseous phase P_g is obtained from the readings of the mass balance on dry air.

$$\gamma_1\left(\frac{\partial T}{\partial t}\right)+\gamma_2\left(\frac{\partial W}{\partial t}\right)+\gamma_3\left(\frac{\partial P_g}{\partial t}\right) \\ = -\nabla\cdot(D_a^T\nabla T+D_a^W\nabla W+D_a^P\nabla P_g+D_a^g g) \tag{12}$$

The last equation on temperature T matches the relation (10).

$$\overline{\rho C_p}\frac{\partial T}{\partial t}+\begin{pmatrix}(D_l^T\nabla T+D_l^W\nabla W+D_l^P\nabla P_g+D_l^g g)C_{p_l}\\ +(D_a^T\nabla T+D_a^W\nabla W+D_a^P\nabla P_g+D_a^g g)C_{p_a}\\ +(D_v^T\nabla T+D_v^W\nabla W+D_v^P\nabla P_g+D_v^g g)C_{p_v}\end{pmatrix}\cdot\nabla T \\ +\nabla\cdot(-\lambda^*\nabla T)+K(\Delta H_v+\Delta H_b)=\phi_{so} \tag{13}$$

where the phase change rate K is given by the following relation:

$$K=\nabla\cdot(D_v^T\nabla T+D_v^W\nabla W+D_v^P\nabla\overline{P}_g^g+D_v^g g) \tag{14}$$

2.1.3. Boundary conditions

Referring to Fig. 1, the continuity of the surface heat flux ($x = 0$) is given by the relation (15). For the bottom side ($x = L$) of the sample, one can introduce two conditions: an adiabatic wall (relation (16)) or an isothermal wall (relation (17)).

$$-\lambda^*\nabla T+\rho_l\overline{V}_l(\Delta H_v+\Delta H_b) \\ = h_c(T_a-T(0,t))+h_r(T_p-T(0,t)) \tag{15}$$

$$-\lambda^*\nabla T+\rho_l\overline{V}_l(\Delta H_v+\Delta H_b)=0 \tag{16}$$

$$T(L,t)=T \tag{17}$$

The mass transfers read as follows:

$$\text{At } x=0,\quad -(\bar{\rho}_v^g\overline{V}_v+\rho_l\overline{V}_l)=F_m \qquad \text{with} \\ F_m=k_m\frac{P_{atm}M_v}{RT_f}\ln\left(\frac{P_{atm}-P_{v\infty}}{P_{atm}-P_v(0,t)}\right) \tag{18}$$

The mass coefficient k_m is determined using Colburn analogy [20].

At $x = L$, the surface is impermeable

$$\bar{\rho}_g^g\overline{V}_g=0 \quad \text{and} \quad \rho_l\overline{V}_l=0 \tag{19}$$

The pressure at the upper side of the sample is considered equal to the atmospheric pressure.

2.2. Energy inputs by electromagnetic radiation

Calculation of energy inputs induced by radiating sources within the supposedly homogeneous material hinges on the simplified representation given by the Lambert–Beer law [20]:

$$\Phi_x^t=\Phi_{x=0}^t e^{-\kappa x}=(1-R)\Phi^i e^{-\kappa x} \tag{20}$$

This assumption is justified by the experimental conditions. Infrared emitter is positioned on the upper sample (Fig. 2). The microwave radiations penetrate only through the upper side of the material because an adhesive metal piece is fitted on the others faces.

The values of the reflection and attenuation coefficients, respectively R and κ, depend on the thermal-optic properties of the material in the case of infrared radiation and on dielectric properties in the case of microwaves. The absorbed power on a δx thickness of material is thus given by the following equation:

$$\Phi_{\delta x}^a=\Phi_x^t-\Phi_{x+\delta x}^t=(1-R)\Phi^i(e^{-\kappa x}-e^{-\kappa(x+\delta x)}) \\ =(1-R)\Phi^i e^{-\frac{x}{d}}\left(1-e^{-\frac{\delta x}{d}}\right) \tag{21}$$

in which d is the penetration depth.

2.2.1. Infrared radiation

The emission spectrum of industrial emitters is in the 0.8–10 μm range [1]. In the case of an opaque material, the penetration depth reaches a few microns. Infrared will thus induce a superficial heating, the heat being then transmitted by conduction through the material. The absorbed heat flux is given by the following equation:

$$\Phi^a=\Phi_{x=0}^t=\alpha\Phi^i \tag{22}$$

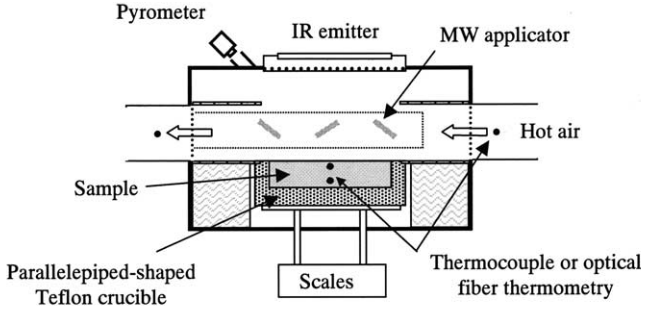

Fig. 2. Experimental diagram.

α being the absorption coefficient, which depends on the superficial moisture content and on the wavelength range of the incident lighting. Afterwards, the studied material will be assimilated to a grey body with diffuse emission and reflection.

With industrial-type infrared emitters, one can apply a very high irradiation to the product. In that case, these inputs must therefore be kept under control in order to avoid deteriorating the material or else lead to caking phenomena [11].

2.2.2. Microwave radiation

As for microwave heating, generators work at a frequency of 2.45 GHz or 900 MHz. The penetration depth d of the electromagnetic wave can be approximated by the following relation [1]:

$$d = \frac{1}{\kappa} = \frac{\lambda_0 \varepsilon'_r}{2\pi\varepsilon''_r\sqrt{\varepsilon'_r}} \tag{23}$$

This evolves throughout the drying process, as the dielectric permittivity ε'_r and the relative loss factor ε''_r are closely related to the moisture content and the temperature. The approximated value of the reflection coefficient R is given by the following relation:

$$R = \left(\frac{1-\sqrt{\varepsilon'_r}}{1+\sqrt{\varepsilon'_r}}\right)^2 \tag{24}$$

During the simulation, the dielectric parameters are determined according to the mean moisture content of the sample. Microwaves are efficient in that they allow immediately significant energy input to the core of the product. The thermal properties of the material do not influence the heat generation. In this context, only its dielectric properties are relevant [5,13].

2.3. Numerical solution procedure

Spatial discretisation of the sample is ensured according to the control volume method developed by Patankar [21]. The calculation field is uniformly divided in control volumes. Eqs. (11)–(13) are integrated to these volumes then discretised with a linear interpolation. Physical properties are supposed constant in each control volume and determined by an arithmetic average at the interfaces, except for the thermal conductivity, which requires a harmonic average. Thus one obtains three systems of ordinary differential equations, that remain to be solved, The temporal resolution of each system is achieved by means of an implicit scheme. Treating nonlinearity and coupling of the three equation systems, one uses an iterative algorithm [22]. Convergence of calculations is ensured by introducing three relative criteria for each state variable.

3. Experimental device

The experimental chamber was made of non-magnetic stainless steel and had an inside volume of 38 dm^3 (Fig. 2). Coupled with this chamber were a short infrared source, a microwave applicator and an air-heating loop [23].

Various fittings were required in order to meet one-dimensional heat and mass transfer conditions. First, the sample of thickness 1 or 2.5 cm according to study is placed in a parallelepiped-shaped Teflon crucible of section 10 cm × 10 cm. The air flux on the upper side is funnelled through a rectangular casing and is stabilised by a convergent duct placed at the entrance of the kiln. Besides, both lateral and bottom faces of the crucible are insulated, and a stainless steel tube, in which water circulates at a temperature similar to this of the material, is fitted around the crucible. This device allows approaching adiabatic and impermeable conditions for surfaces, which are not in contact with the drying air. The sample holder is placed on a tripod, itself resting on scales permitting a constant monitoring of the product mass.

The infrared radiation source is placed on the upper side of the kiln. It consists of two emitters of standard industrial type, each developing 1 kW and working in the short infrared range. As for dielectric heating, a generator of 1.2 kW nominal power working at 2.45 GHz is used. This is coupled with a waveguide with radiating slits situated on the backside of the kiln. The unit kiln-waveguide forms a multimode applicator.

This drying pilot allows monitoring of the promptings applied to the product and following through the evolution of its temperature and mass. During tests of plain convective drying or otherwise tests combining convection and infrared, temperatures within the material are recorded by thermocouples. Optical fibre thermometry is used in the presence of microwaves. Surface temperature is measured by means of an optical pyrometer.

4. Results and discussion

The results given in this paper were obtained with samples of cellular concrete of a 10^{-2} cm^2 section and a thickness of 1 or 2.5 cm. Autoclaved cellular concrete was chosen as experimental material because of its industrial manufacture, which guarantees fairly consistent thermophysical characteristics. Besides, this product is abundantly documented [6]. It is an extremely porous hygroscopic material ($\varepsilon = 0.8$).

All simulations presented in this paper use a grid size of 0.125 cm and a time stepping of 0.01 s. For stopping iterative processes, the absolute convergence criteria are calculated on the control volumes. The values for temperature, pressure and moisture content are respectively 10^{-3} °C, 10 Pa and 10^{-4} $\mathrm{kg\,kg^{-1}}$. Moreover, the convection term in the heat equation as well as the terms of gravity are neglected [24].

The initial conditions are defined by the experiment and the solicitations applied to the surface (air temperature, hygrometry and microwave power) correspond to measures conducted in real time. For incident infrared irradiation, measures previously obtained with a sensor developed in our laboratory [25] are used. The infrared absorption coefficient α was then deduced from a heat balance during a drying test. The coefficient reaches a value of 0.7 during the constant drying rate period and of 0.5 afterwards. The convective exchange coefficient is determined experimentally at constant air velocity. Dielectric properties evolve with the moisture content and are taken in the literature [13].

4.1. Convective drying

4.1.1. Study at 60 °C, $H_r = 6\%$

An experiment is performed on a 1 cm thick sample with a temperature and an air velocity of 60 °C and 3 $\mathrm{m\,s^{-1}}$ respectively. The first simulation was conducted considering an adiabatic condition on the bottom side of the sample ($x = L$). Fig. 3(a) shows evolution of the moisture content in the material. The good convergence of the calculation can be noted with the progression of the evaporation front, from the surface towards the bottom of the sample. About the gaseous phase pressure, evolutions obtained are in accordance with those presented by Turner [5]. The pressure within the material increases after the is enthalpy phase (Fig. 3(b)) and cancels itself at the end of drying. On these plottings, oscillations are caused by the discontinuity of the permeability models [24]. The corresponding evolutions of temperatures taken at the surface level and at a depth of 0.5 cm are presented in Fig. 3(c). These simulated results are agree with adiabatic conditions: the whole temperatures converge towards 60 °C, i.e. the air temperature. On the other hand, the adiabatic wall condition does not correctly match the experimental conditions. Indeed, Fig. 3(c) shows discrepancies that can reach up to 10 °C between calculated temperatures and those measured at a depth of 0.5 cm. Moreover, the evolution of the simulated mean moisture content does not correctly match the experiment, particularly in the beginning of the drying phase. Thus, a second simulation, imposing at a depth of $x = L$ the measured temperature values is performed. In this case we obtained good agreement between measured and calculated values for temperatures and mean moisture contents (Fig. 4). On this figure, the constant drying rate period is perceptible during 150 min. The surface temperature is equal to the wet bulb temperature. The liquid migration inside the material to the surface leads to make uniform the temperature distribution of the sample by capillary action. At the end of this period, the surface temperature increases due to the diminution of water activity. Then, the evaporation front penetrates inside the material as we can see on the figure. The results obtains at 0.5 cm depth show that the temperature marks a second stage.

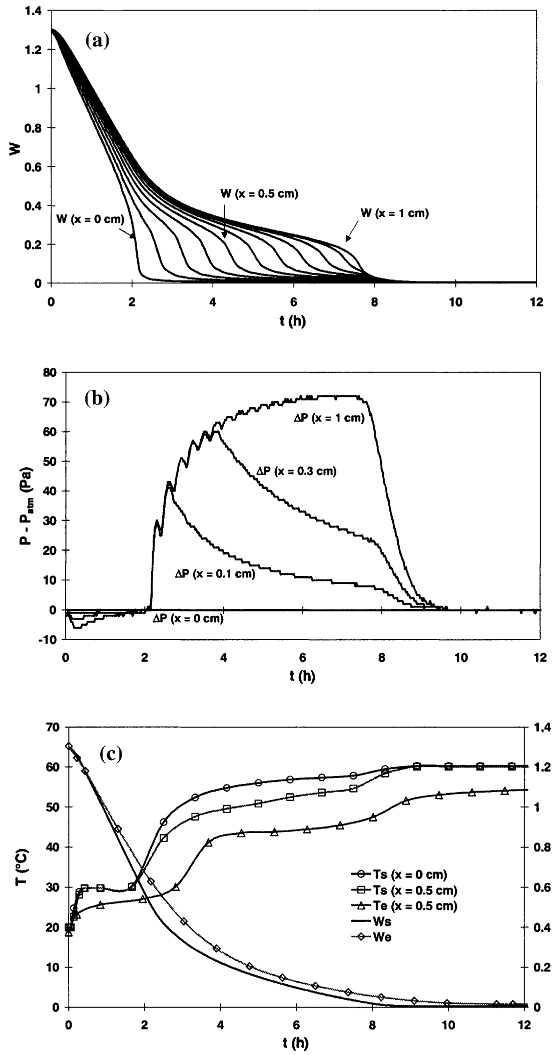

Fig. 3. Convective drying at 60 °C with an adiabatic condition on the bottom of the sample: (a) Predicted moisture content profiles within the material. (b) Evolution of overpressures within the material. (c) Comparison of experimental "e" and simulated "s" temperature and average moisture content profiles in time.

These first results show a good calculation convergence and sensitivity of the model in relation with boundary conditions. Afterwards, the Dirichlet condition is applied.

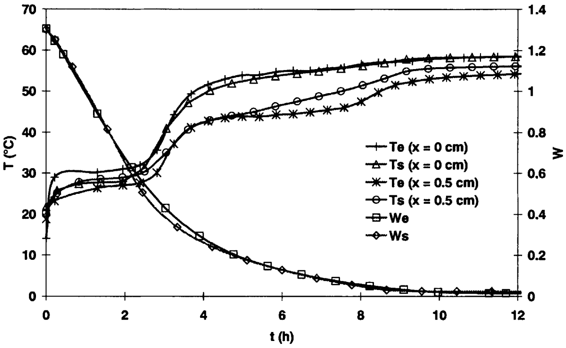

Fig. 4. Convective drying at 60 °C, imposing at $x = L$ the measured temperature values. Comparison of experimental "e" and simulated "s" temperature and average moisture content profiles in time.

4.1.2. Study at 80 °C, $H_r = 3\%$

In order to confirm the previous results, a test conducted at an air temperature of about 80 °C and with a 2.5 cm thick sample is presented here. Fig. 5(a) illustrates the comparison between experimental and calculated evolutions of temperature at surface level and at a depth of 2 cm. The results are very satisfying. That is the same thing for the average moisture content. Moreover, as shown on Fig. 5(b), the increase in sample thickness and air temperature give an increase in overpressure values. Compared with the previous simulation (Fig. 3(b)), due to smoothing of the calculated values, the plottings do not show any oscillation. In order to quantify the contribution of pressure gradients, another simulation was conducted without introducing the pressure equation in the model. In this case, Fig. 5(a) shows a decrease in mean moisture content, slower but rather insignificant. This result tallies with the rest of the scientific literature, where chosen models do not feature pressure equations during simulation of purely convective drying operations.

4.2. Infrared and convective drying

To study this combination, we present a test conducted on a 2.5 cm thick sample with an air temperature fixed at 30 °C and an hygrometry at 25%. Surface temperature is maintained at 70 °C throughout the experiment by means of intermittently activated infrared emitters. The maximum irradiation applied to the material was 8 kW m^{-2}. Fig. 6(a) shows the experimental conditions, the infrared power received by the material

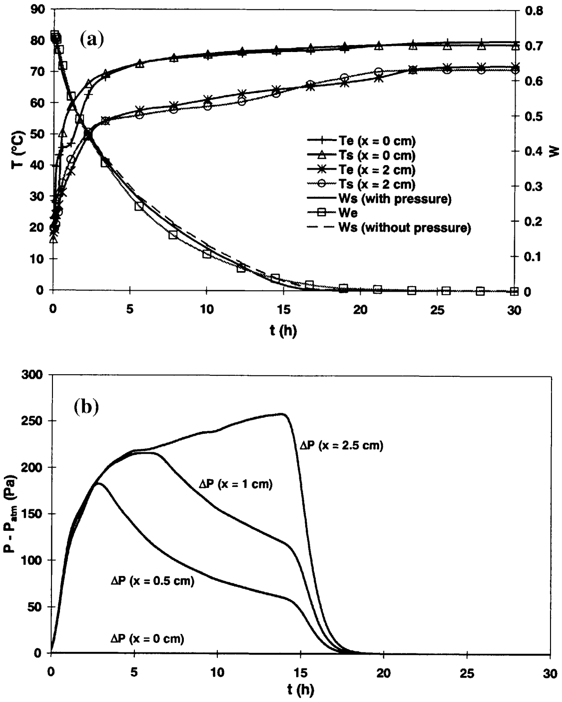

Fig. 5. Convective drying at 80 °C: (a) comparison of experimental "e" and simulated "s" temperature and average moisture content profiles in time with and without introducing the pressure equation, (b) predicted evolution of overpressures within the material.

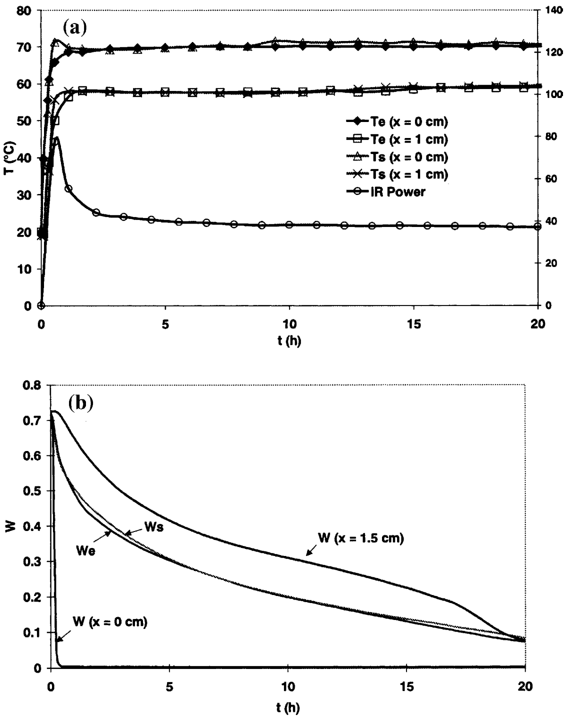

Fig. 6. Infrared and convection drying: (a) IR means power. Comparison of experimental "e" and simulated "s" temperature profiles in time. (b) Comparison of experimental "e" and simulated "s" moisture content profiles in time.

and the corresponding temperature response. These plottings correspond to averaged values due to the intermittent character of infrared irradiation. We thus obtained very satisfying results, nearing measured values. As far as temperatures are concerned, the diversion is only of a few degrees at material surface before stabilising at 70 °C. As for the water content, the simulated drying kinetic is very close to the experimental kinetic, as shown in Fig. 6(b). Compared with the convection tests, the simulation highlights a very rapid superficial drying (< 30 min). This phenomenon results in slowing down the drying of the material. The evaporated mass flow, which is directly linked with the surface water activity, drops as soon as the moisture content at saturation point is reached.

4.3. Microwave and convective drying

The thickness of the material remains 2.5 cm and the air temperature is fixed at 30 °C ($H_r = 25\%$). During this experiment, the temperature at a depth of 1 cm is maintained at 70 °C by an intermittent use of the microwave generator. At the beginning of the drying process, the power introduced in the kiln is of 160 W (Fig. 7(a)). One must note that an adhesive metal piece is fitted around the crucible in order to have the radiation penetrating solely through the upper side of the material.

Compared with the previous tests, the observation of Fig. 7(a) shows an inversion of the temperature gradients in the material, correctly featured by the model. To obtain this simulation result, two permeability models (k_{rl}, k_{rg}) developed by Moyne [24] were tested. Fig. 7(b) shows the influence of these models on the moisture content evolution. In this case, the relative permeabilities giving the least importance to the transfers in the liquid phase (Fig. 8) give results that are the closest to the experimental evolution (Fig. 7(b)). As for the local moisture contents, one notices an increase in moisture content at the bottom of the sample at the beginning of the drying process. This phenomenon is caused by the important overpressures at the centre of the sample, corresponding to the maximum temperature (Fig. 7(c)). When a significant moisture content is matched with a high core temperature, this tends to cause significant pressure gradients.

In spite of its simplicity, the electromagnetic heat generation model proves efficient and gives a good picture of the phenomena. Moreover, introducing microwaves highlights the importance of choosing the relative permeabilities model, compared with convective drying.

4.4. Combined microwave, infrared and convective drying

In order to test the validity of the model during a combined drying operation, a test conducted with a 2.5 cm thick sample and an air temperature of 30 °C

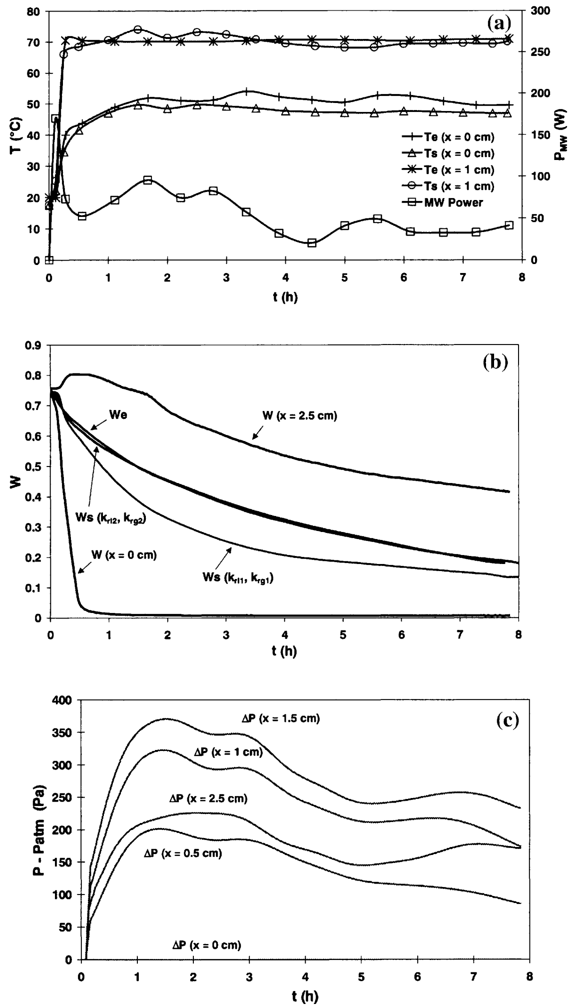

Fig. 7. Microwave and convection drying: (a) MW absorbed power. Comparison of experimental "e" and simulated "s" temperature profiles in time. (b) Evolution of experimental "e" and simulated "s" local and means moisture content profiles in time. (c) Overpressure profiles in time within the material.

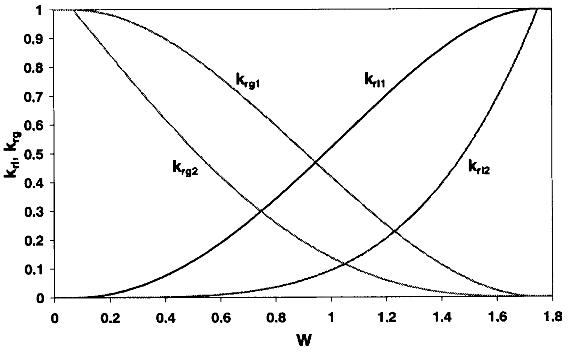

Fig. 8. Relative permeability models for liquid (k_{rl}) and gaseous (k_{rg}) phases according to moisture (Moyne [24]).

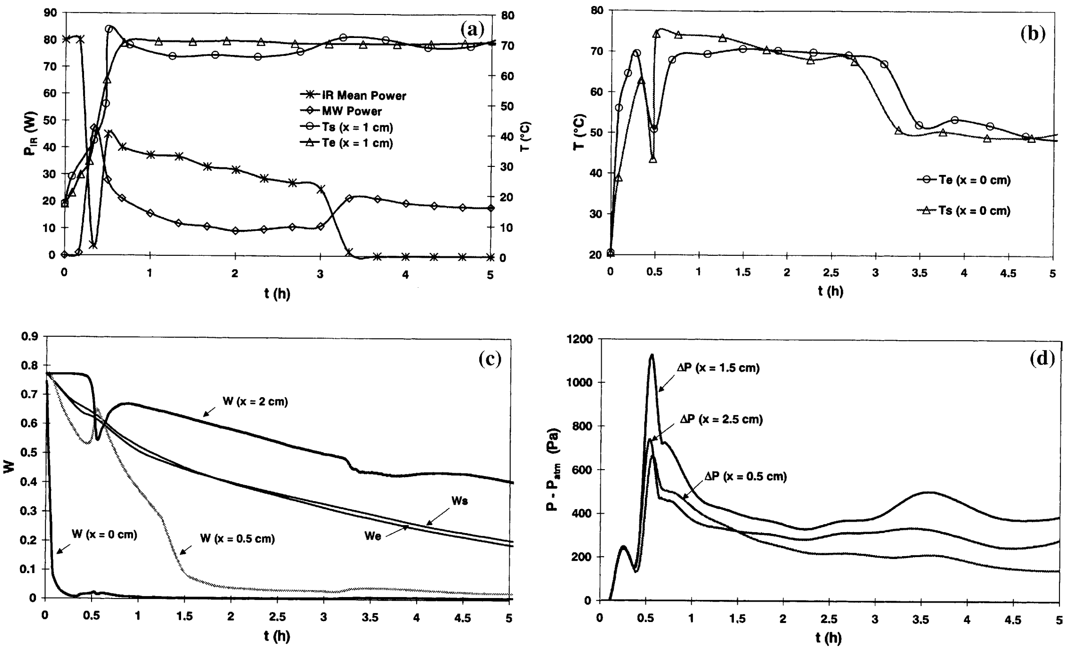

Fig. 9. Combined microwave, infrared and convection drying. (a) Evolution of means absorbed MW and IR power. (b) Evolution of experimental "e" and simulated "s" temperature profiles in time at surface level. (c) Evolution of experimental "e" and simulated "s" moisture content profiles in time. (d) Overpressures profiles in time within the material.

($H_r = 25\%$) is used as database. During this experiment, the material temperature is maintained at 70 °C, but simultaneous use of both radiating sources is excluded. Infrared are applied in the beginning of the drying and cease to be used as soon as the average water content of the product drops under 0.3, which shows a very low activity of surface water (Fig. 9(a)).

The model correctly reproduces the experimental conditions. The simulated temperatures are in agreement with the measures. The gradient between the surface and the core of the material is found again as soon as the incident infrared irradiation is interrupted (Fig. 9(a) and (b)). Besides, the evolution of local moisture contents clearly shows the various phenomena at play (Fig. 9(c)). Infrared used in the beginning of the process allows a rapid raise in surface temperature and thus of corresponding steam pressure. Consequently, evaporation is boosted and evacuated mass flux rapidly. When surface temperature reaches the selected value 70 °C, microwaves take over from infrared. Under volume heating, the water emerging from the core of the product migrates to the surface. Significant overpressures occur at the core of the material (Fig. 9(d)), which activates the movement of water towards the surface. As soon as the internal temperature stabilises itself at around 70 °C, the infrared radiation is reactivated, which permits rapid evaporation. Throughout this period, infrared and microwaves work intermittently and the temperature gradient between the surface and the core of the material is then negligible. When the water content reaches the 0.3 kg kg^{-1} value, the infrared emitter is turned off. Then a decrease in surface temperature is observed.

One should note that the combination of these two types of radiation shorten the drying period. Applying microwaves considerably increases mass transfers from the inside towards the surface and infrared permit activating evaporation.

5. Conclusions

The modeling of the hygrothermal behaviour of a porous medium submitted to infrared and microwave radiations has been presented in this paper. A one-dimensional heat and mass transfers model is used. The electromagnetic power absorbed was assumed to decay exponentially into the sample following the Lambert–Beer law. The simulations give the evolution of moisture content, temperature and total pressure of the gaseous phase during combined drying.

Tests conducted on cellular concrete showed that the simulations results are in good agreement with measures obtained in an experimental kiln. The simplified expression of the microwave source term leads to a satisfying representation of the complex phenomena at play. Besides, the simulations have showed the sensitivity of the model to relative permeabilities, when microwave and convection are combined.

The presented results have shown the relative influence of each electromagnetic source on the evolution of water content and on the temperature response of the material. Using infrared in the early drying phase stages allows a rapid rise of the surface temperature, which significantly increases the saturating steam pressure, thus activating evaporation. However, as soon as the surface dries up, this advantage vanishes. As far as microwaves are concerned, the important penetration depth allow inducing overpressures at the core of the material, thus boosting the transfer of the existing water from the core to the surface.

In conclusion, the aim of this work is to study the potential advantages resulting from the introduction of radiating sources in a convective drying process. We will now concentrate on optimizing the operation of these sources by integrating various criteria into the process and the product.

Appendix A. Flux expressions

Liquid flux

$$\mathbf{J}_{\mathrm{l}} = \rho_{\mathrm{l}}\overline{\mathbf{V}}_{\mathrm{l}} = D_{\mathrm{l}}^{T}\nabla T + D_{\mathrm{l}}^{W}\nabla W + D_{\mathrm{l}}^{P}\nabla P_{\mathrm{g}} + D_{\mathrm{l}}^{\mathrm{g}}\mathbf{g}$$

Vapour flux

$$\mathbf{J}_{\mathrm{v}} = \bar{\rho}_{\mathrm{v}}^{\mathrm{g}}\overline{\mathbf{V}}_{\mathrm{v}} = D_{\mathrm{v}}^{T}\nabla T + D_{\mathrm{v}}^{W}\nabla W + D_{\mathrm{v}}^{P}\nabla P_{\mathrm{g}} + D_{\mathrm{v}}^{\mathrm{g}}\mathbf{g}$$

Air flux

$$\mathbf{J}_{\mathrm{a}} = \bar{\rho}_{\mathrm{a}}^{\mathrm{g}}\overline{\mathbf{V}}_{\mathrm{a}} = D_{\mathrm{a}}^{T}\nabla T + D_{\mathrm{a}}^{W}\nabla W + D_{\mathrm{a}}^{P}\nabla P_{\mathrm{g}} + D_{\mathrm{a}}^{\mathrm{g}}\mathbf{g}$$

A.1. Vapour flux

$$D_{\mathrm{v}}^{T} = -D_{\mathrm{v}}^{\mathrm{eff}}\left(\frac{M_{\mathrm{a}}M_{\mathrm{v}}}{MRT}\right)\left(\frac{\partial P_{\mathrm{v}}}{\partial T}\right)$$

$$D_{\mathrm{v}}^{W} = -D_{\mathrm{v}}^{\mathrm{eff}}\left(\frac{M_{\mathrm{a}}M_{\mathrm{v}}}{MRT}\right)\left(\frac{\partial P_{\mathrm{v}}}{\partial W}\right)$$

$$D_{\mathrm{v}}^{P} = -\left[\bar{\rho}_{\mathrm{v}}^{\mathrm{g}}\frac{kk_{\mathrm{rg}}}{\mu_{\mathrm{g}}} - D_{\mathrm{v}}^{\mathrm{eff}}\left(\frac{M_{\mathrm{a}}M_{\mathrm{v}}}{MRT}\right)\frac{P_{\mathrm{v}}}{P_{\mathrm{g}}}\right]$$

$$D_{\mathrm{v}}^{\mathrm{g}} = \bar{\rho}_{\mathrm{v}}^{\mathrm{g}}\bar{\rho}_{\mathrm{g}}^{\mathrm{g}}\frac{kk_{\mathrm{rg}}}{\mu_{\mathrm{g}}}$$

A.2. Dry air flux

$$D_{\mathrm{v}}^{T} = D_{\mathrm{v}}^{\mathrm{eff}}\left(\frac{M_{\mathrm{a}}M_{\mathrm{v}}}{MRT}\right)\left(\frac{\partial P_{\mathrm{v}}}{\partial T}\right) = -D_{\mathrm{v}}^{T}$$

$$D_{\mathrm{a}}^{W} = D_{\mathrm{v}}^{\mathrm{eff}}\left(\frac{M_{\mathrm{a}}M_{\mathrm{v}}}{MRT}\right)\left(\frac{\partial P_{\mathrm{v}}}{\partial W}\right) = -D_{\mathrm{v}}^{W}$$

$$D_{\mathrm{a}}^{P} = -\bar{\rho}_{\mathrm{a}}^{\mathrm{g}}\frac{kk_{\mathrm{rg}}}{\mu_{\mathrm{g}}} - D_{\mathrm{v}}^{\mathrm{eff}}\left(\frac{M_{\mathrm{a}}M_{\mathrm{v}}}{MRT}\right)\frac{P_{\mathrm{v}}}{P_{\mathrm{g}}}$$

$$D_{\mathrm{a}}^{\mathrm{g}} = \bar{\rho}_{\mathrm{a}}^{\mathrm{g}}\bar{\rho}_{\mathrm{g}}^{\mathrm{g}}\frac{kk_{\mathrm{rg}}}{\mu_{\mathrm{g}}} = \frac{\bar{\rho}_{\mathrm{a}}^{\mathrm{g}}}{\bar{\rho}_{\mathrm{g}}^{\mathrm{g}}}D_{\mathrm{v}}^{\mathrm{g}}$$

A.3. Liquid flux

$$D_{\mathrm{l}}^{T} = \rho_{\mathrm{l}}\frac{kk_{\mathrm{rl}}}{\mu_{\mathrm{l}}}\left(\frac{\partial P_{\mathrm{c}}}{\partial T}\right)$$

$$D_{\mathrm{l}}^{W} = \rho_{\mathrm{l}}\frac{kk_{\mathrm{rl}}}{\mu_{\mathrm{l}}}\left(\frac{\partial P_{\mathrm{c}}}{\partial W}\right)$$

$$D_{\mathrm{l}}^{P} = \rho_{\mathrm{l}}\frac{kk_{\mathrm{rl}}}{\mu_{\mathrm{l}}}\left(\frac{\partial P_{\mathrm{c}}}{\partial P_{\mathrm{g}}}\right) - \rho_{\mathrm{l}}\frac{kk_{\mathrm{rl}}}{\mu_{\mathrm{l}}}$$

$$D_{\mathrm{l}}^{\mathrm{g}} = \rho_{\mathrm{l}}\frac{kk_{\mathrm{rl}}}{v_{\mathrm{l}}}$$

A.4. Coefficients of pressure equation

$$\gamma_1 = \varepsilon\frac{M_{\mathrm{a}}}{RT}(1-S)\left(\frac{P_{\mathrm{v}}-P_{\mathrm{g}}}{T} - \frac{\partial P_{\mathrm{v}}}{\partial T}\right)$$

$$\gamma_2 = -\frac{\varepsilon M_{\mathrm{a}}}{RT}(1-S)\left[\frac{\partial P_{\mathrm{v}}}{\partial W} + \rho_s\frac{(P_{\mathrm{g}}-P_{\mathrm{v}})}{\rho_{\mathrm{l}}\varepsilon(1-S)}\right]$$

$$\gamma_3 = \varepsilon\frac{M_{\mathrm{a}}}{RT}(1-S)$$

with M_{g}, the density of the gaseous phase $\left(M_{\mathrm{g}} = \frac{P_{\mathrm{a}}M_{\mathrm{a}}+P_{\mathrm{v}}M_{\mathrm{v}}}{P_{\mathrm{g}})}\right.$ and S, the saturation $\left(S = \frac{W\rho_{\mathrm{s}}}{\varepsilon\rho_{\mathrm{l}}}\right)$.

References

[1] A.C. Metaxas, Foundations of Electroheat, Wiley, Chichester, 1996.

[2] J. Thuéry, Les Micro-ondes et Leurs Effets sur la Matière, second ed., Lavoisier, Paris, 1989.

[3] M. Dostie, Optimization of a drying process using infrared, radio frequency and convection heating, Drying'92, Elsevier Science Publishers, 1992, pp. 679–684.

[4] A.K. Datta, H. Ni, Infrared and hot-air-assisted microwave heating of foods for control of surface moisture, J. Food Eng. 51 (2002) 336–364.

[5] I.W. Turner, P.G. Jolly, Combined microwave and convective drying of a porous material, Drying Technol. 9 (5) (1991) 1209–1269.

[6] T. Constant, P. Perré, C. Moyne, Microwave drying of light concrete: from transport mechanisms to explanation of energy savings, in: A.S. Mujumdar (Ed.), Drying'92, 1992, pp. 617–626.

[7] P. Perré, I.W. Turner, The use of numerical simulation as a cognitive tool for studying the microwave drying of softwood in an over-sized waveguide, Wood Sci. Technol. 33 (1999) 445–464.

[8] M.A. Roques, F. Zagrouba, Analysis of heat and mass fluxes during microwave drying, Drying Technol. 15 (9) (1997) 2113–2127.

[9] I.W. Turner, J.R. Puigalli, W. Jomma, A numerical investigation of combined microwave and convective drying of a hygroscopic porous material: A study based on pine wood, Trans. IChemE 76 Part A (1998) 193–209.

[10] P. Ratanadecho, K. Aoki, M. Akahori, Experimental and numerical study of microwave drying in unsaturated

porous material, Int. Commun. Heat Mass Transfer 28 (5) (2001) 605–616.

[11] P. Navarri, Etude du séchage par rayonnement infrarouge: application à un produit capillaro-poreux et à une enduction, PhD thesis, University Lyon I, France, 1992.

[12] P. Navarri, J. Andrieu, A. Gevaudan, Studies on infrared and convective drying of non-hydroscopic solids, in: A.S. Mujumdar (Ed.), Drying'92, 1992, pp. 685–694.

[13] T. Constant, Le séchage combiné convection-microondes: Modélisation–Validation–Optimisation, PhD thesis, INPL, France, 1992.

[14] S. Whitaker, Simultaneous heat, mass, and momentum transfer in porous media: a theory of drying, Adv. Heat Transfer 54 (1977) 13.119–13.203.

[15] F. Couture, Modélisation fine d'un problème de séchage, développement d'outils adaptés, PhD thesis, University Bordeaux I, France, 1995.

[16] J.M. Courivaud, G. Bacon, P. Crausse, Simulation numérique d'un béton cellulaire dans sa phase d'élaboration sous gradient de pression de vapeur à haute température, Revue Générale de Thermique 36 (1997) 264–275.

[17] C. Moyne, P. Perré, Processes related to drying: Part I, Theoretical model, Drying Technology 9 (5) (1991) 1135–1152.

[18] P. Perré, C. Moyne, Processes related to drying: Part II, Use of the model to solve transfers both in saturated and unsaturated porous media, Drying Technol. 9 (5) (1991) 1153–1179.

[19] J. Nadeau, J.-R. Puiggali, Séchage des processus physiques aux procédés industriels, Tec. & Doc, Lavoisier, 1995.

[20] J.P. Holmann, Heat Transfer, seventh ed., McGraw-Hill, 1990.

[21] S.V. Patankar, Numerical Heat Transfer and Fluid Flow, Hemisphere Publishing Corporation, New York, 1980.

[22] D. Lecharpentier, Optimisation d'un procédé de séchage, Problématiques liées au transfert de masse et de chaleur lors de l'utilisation de technologies rayonnantes micro-onde et infrarouge, PhD thesis, University Nantes, France, 2000.

[23] P. Glouannec, D. Lecharpentier, H. Noël, Experimental survey on the combination of radiating infrared and microwave sources for the drying of porous material, Appl. Therm. Eng. 22 (2002) 1689–1703.

[24] C. Moyne, Transferts couplés chaleur-masse lors du séchage: prise en compte du mouvement de la phase gazeuse, PhD thesis, INPL, France, 1987.

[25] H. Noël, J.P. Ploteau, P. Glouannec, Thermoelectric device for infrared radiation measurements, in: Proceedings of the 8th International Symposium on Temperature and Thermal Measurements in Industry and Science, Verlag, Berlin, 2001, pp. 925–930.